Journal of Applied Physics

RESEARCH ARTICLE | JULY 23 2024

Correlation of heat transport mechanism and structural properties of GaN high electron mobility transistors

Lisa Mitterhuber ; Barbara Kosednar-Legenstein ; Anurag Vohra ; Matteo Borga ; Niels Posthuma ; Elke Kraker

J. Appl. Phys. 136, 045108 (2024)
https://doi.org/10.1063/5.0207513

19 September 2024 08:56:25

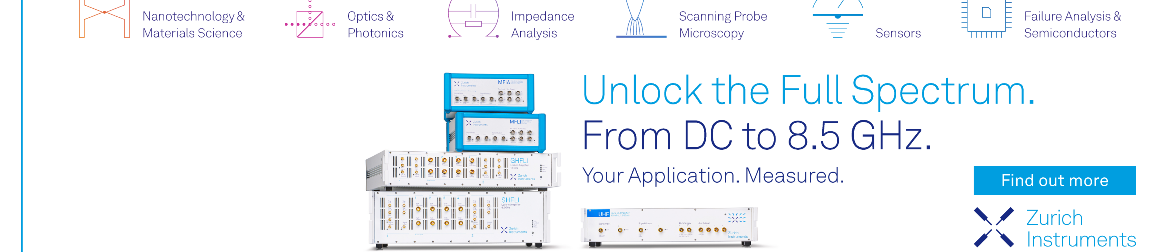

Journal of Applied Physics ARTICLE pubs.aip.org/aip/jap

Correlation of heat transport mechanism and structural properties of GaN high electron mobility transistors

Cite as: J. Appl. Phys. **136**, 045108 (2024); doi: 10.1063/5.0207513
Submitted: 8 March 2024 · Accepted: 28 June 2024 ·
Published Online: 23 July 2024

Lisa Mitterhuber,[1,a)] Barbara Kosednar-Legenstein,[1] Anurag Vohra,[2] Matteo Borga,[2] Niels Posthuma,[2] and Elke Kraker[1]

AFFILIATIONS

[1]Materials Center Leoben Forschung GmbH, Roseggerstraße 12, 8700 Leoben, Austria
[2]Imec, Kapeldreef 75, Leuven 3001, Belgium

[a)]**Author to whom correspondence should be addressed:** lisa.mitterhuber@mcl.at

ABSTRACT

Grain sizes, impurities, and layer thicknesses in the nm-range affect the heat transport and, hence, hinder proper heat dissipation of GaN-based devices. To obtain a clear picture of heat dissipation, the mechanisms of heat transport must be linked to the structural properties of the nitride-based materials in the device. In this paper, a systematic investigation of the typical layers of GaN high-electron mobility transistor stacks was conducted by time-domain thermoreflectance analysis and Raman measurements. The analyzed layers are the AlN nucleation layer, the $Al_{0.3}Ga_{0.7}N$ transition layer, the AlGaN/AlN superlattice, the C-doped GaN back-barrier, and the uid GaN layer. The results were interpreted using the Born–van Karman model, including the suppression function approach to describe the governing heat transport mechanisms. Investigation of this AlN nucleation layer showed that its phonon scattering is dominated by impurity and grain boundary scattering. The $Al_{0.3}Ga_{0.7}N$ transition layer was shown to have a reduced thermal conductivity not only due to alloy scattering but also because of grain boundary scattering. The AlGaN/AlN superlattice showed a thermal conductivity lower than the $Al_{0.3}Ga_{0.7}N$ transition layer, especially at higher temperatures (7.2 ± 0.2 W/mK vs 14.1 ± 0.4 W/mK at 300 °C). Caused by the enhanced AlGaN/AlN interface density, the thermal conductance was found to be 2 GW/m^2 K. The AlGaN/AlN superlattice indicated an anisotropic thermal transport with a factor of ∼1.5. The C-doped GaN layers were analyzed in terms of their size-dictated thermal conductivity, resulting in a reduction of ∼66% from 1 μm to 250 nm at 30 °C. Raman spectroscopy revealed that the thicker the GaN layer, the higher the compressive stress in GaN, which additionally results in a higher thermal transport. The investigations of the heat transport depending on the structural properties enabled an accurate determination of the thermal conductivity of the layer stack. These thermal conductivities served as input parameters for 3D simulation to extract the temperature, in terms of the thermal resistance, of such high-electron mobility transistor stacks. This simulation shows the importance of the GaN layer in terms of thermal management. This work uncovers the thermal transport in GaN-based transistor stacks with the aim to improving the thermal design.

© 2024 Author(s). All article content, except where otherwise noted, is licensed under a Creative Commons Attribution (CC BY) license (https://creativecommons.org/licenses/by/4.0/). https://doi.org/10.1063/5.0207513

19 September 2024 08:56:25

I. INTRODUCTION

High-electron mobility transistors (HEMTs), using the aluminum gallium nitride (AlGaN)/gallium nitride (GaN) heterojunction, have already proven their capabilities in handling high-power and high-frequencies. It already offers a cost-alternative solution for mid-power HEMTs when the heterojunction is produced on Si.[1] However, performance degradation and reliability concerns are still an issue in these systems. A prominent example is self-heating, which affects the electron mobility in the channel and, hence, lowers the carrier transport. This degrades the direct current (DC) and radio frequency (RF) characteristics.[2] It becomes even more pronounced in such systems as they are operated at high-power densities, which additionally poses a reliability issue, since the device's reliability and performance go hand in hand with its channel temperature.[3] Hence, the understanding of the generated

© Author(s) 2024

heat and its removal near the junction regions is crucial to utilizing all the above-mentioned benefits of the GaN-based devices.

Several studies have already been conducted to measure the operating temperature of such devices.[4–6] For example, there are electrical methods where the temperature rise of the driven device is determined by its self-heating characteristics.[4] Thermoreflectance measurements were used to map the temperature of the operated HEMT device, enabling it to localize the hottest regions of the surface.[5,6] Also, optical methods like Raman spectroscopy measurements analyze the temperature distribution to find out the thermal resistance of the device.[7–9] All these methods need thermal simulations on top to get an absolute thermal resistance value.[10] These simulations are compared to experiments to reveal the absolute temperature of the GaN-HEMT device under operation.[11] These thermal simulations use literature values, mostly stemming from the bulk values or other manufacturing or application processes. In particular, the presumed values for thermal conductivity must be treated with uncertainty as they could greatly differ from their realistic ones.

With our study, we deliver the accurate thermal conductivity values of materials existing in an AlGaN/GaN-HEMT stack. A systematic study was conducted to investigate the said stack thermally. Thereby, we performed Time-Domain Thermoreflectance (TDTR) measurements together with Raman spectroscopy. The goal of the analysis was to reveal the thermal conductivities of materials and their phonon transport mechanisms used in the HEMT stack. For these calculations, semi-empirical methods were utilized, applying the kinetic equation with the Born–van Karman slack conditions and the assumption of wavelength-dependent boundary scattering. Structural analysis via Raman experiments was set in correlation with the outcome of thermal analysis to deepen the understanding of thermal transport mechanisms. Furthermore, the analyzed thermal conductivity values served further as input parameters for the numerical simulations. These simulations not only provided the operating temperature of a transistor closer to reality but also enabled us to see the potential for improved thermal management, e.g., reduction of GaN layer thickness.

II. EXPERIMENTAL DETAILS

A. Sample preparation

All epitaxial stacks discussed in this study were grown on 200 mm Si (111) substrates using a Veeco MaxBright metalorganic chemical vapor deposition chamber. A schematic of the overall ten different samples is shown in Fig. 1 and Table I. The wafers were cut into $2 \times 2\ \text{cm}^2$ pieces for individual investigations. The investigated samples were typical layers constituting the GaN-HEMT stack grown in a subsequent manner, namely, a 200 nm aluminum nitride (AlN) nucleation layer, a transition layer of 40 nm $Al_{0.3}Ga_{0.7}N$, an AlN/AlGaN superlattice (SL), a carbon (C)-doped GaN back-barrier layer, and a 200 nm unintentionally doped (uid) GaN layer on a silicon (Si) substrate. Hence, Sample 1 (S1)

19 September 2024 08:56:25

FIG. 1. Schematic of the investigated samples; S1 is the Si substrate only with the AlN nucleation layer, whereas S2 has an additional $Al_{0.3}Ga_{0.7}N$ layer on top. S3–S6 differentiate from each other by the thickness of the superlattice (SL) layer and S7–S9 by the thickness of the C-doped GaN layer. S10 consists of full stack with a 200 nm GaN channel, 1 μm C-doped GaN, 1.32 μm SL, 40 nm $Al_{0.3}Ga_{0.7}N$, and a 200 nm AlN nucleation layer.

© Author(s) 2024

TABLE I. List of all samples (S1–S10) with their individual layers and layer thicknesses.

	Layer thickness (nm)									
Layer	S1	S2	S3	S4	S5	S6	S7	S8	S9	S10
AlN	200	200	200	200	200	200	200	200	200	200
$Al_{0.3}Ga_{0.7}N$	…	40	40	40	40	40	40	40	40	40
AlN/AlGaN SL	…	…	165	330	660	1320	1320	1320	1320	1320
C-doped GaN	…	…	…	…	…	…	250	500	1000	1000
uid GaN	…	…	…	…	…	…	…	…	…	200

consisted of the 200 nm AlN on the Si substrate. S2 comprised $Al_{0.3}Ga_{0.7}N$, AlN, and the Si substrate. Samples S3–S6 had the same layer sequence, only differing in the thickness of the superlattice layers. The superlattice was a repetitive layer sequence of AlN and AlGaN, similar to Ref. 12. They differed by the total thickness of the SL, not by the period length, the material underneath, or the material composition. The same applies to samples S7–S9, which had different GaN layer thicknesses. S10 consists of a full buffer stack with a 200 nm GaN channel, 1 μm C-doped GaN, 1.32 μm SL, 40 nm $Al_{0.3}Ga_{0.7}N$, and a 200 nm AlN nucleation layer.

B. Experimental details

The thermal conductivity values and their thermal boundary resistances were obtained by the TDTR measurements setup by PicoTR (Netzsch Japan K.K., Japan). It is an optical pump-probe method, which measures the thermal properties through the change in reflectance with temperature (thermoreflectance). This response is measured as a function of the delay time between the heating pulse of the pump laser (1550 nm, 0.5 ps) and the probe laser pulse (775 nm, 0.5 ps) on the sample's surface. The heating pulses have a repetition rate of 2 MHz. For data acquisition reasons, the pump beam pulses are additionally modulated by 200 kHz via an electro-optic modulator. The probe beam is delayed with respect to the pump beam via an electronic setup. The reflected probe beam as well as the un-reflected probe beam is collected by a differential photodiode, converting the optical signal into electrical signals and further processing by a lock-in amplifier. The phase signal of the lock-in amplifier was used for data processing and thermal evaluation. For the evaluation of the TDTR measurements, a multi-layered approach was used to obtain the thermal conductivity of the material under investigation.[13] The thermal properties of silicon and the used volumetric heat capacity of the individual materials, which were the input parameters of analysis, can be found in the supplementary material. For the alloys and the superlattice, the rule of mixture was applied to calculate the heat capacity. For the TDTR measurements, a sputtered molybdenum (Mo) layer with a thickness of 100 nm was produced on top of all samples afterward. The Mo layer acted as a thermal transducer layer, which is needed for this pump-probe technique (more information in the supplementary material). In this paper, the measurements were carried out at 30 °C, and within the temperature range of 50 and 300 °C, in 50 °C steps. The choice of temperature is in correlation with the typical operating temperature of a HEMT. Each sample at each temperature was measured at three different positions.

A micro-Raman spectrometer was used to determine the structural and crystalline qualities of each sample. The Raman measurements were performed using a confocal micro-Raman spectrometer (WITec alpha300 R, WITec GmbH, Germany) with a 532 nm laser as the excitation source and 1800 g/mm grating. The laser light was focused on the sample surfaces by the 50× EC Epiplan-Neofluar Dic objective (Carl Zeiss AG, Germany). This results in a lateral spatial resolution of <1 μm. A laser power of 15 mW was applied. A spectral shift resolution of ~0.3 cm^{-1} could be achieved by this Raman measurement setup. For Raman stress measurements, calibration of the peak intensity and frequency was done by using an Si wafer.

III. THEORETICAL MODEL

To understand the experimental results, the thermal conductivity was interpreted by the kinetic theory,

$$\kappa = \frac{1}{3}\sum_i \int C(\omega, T)\, v_g^2(\omega)\, \tau_{eff}(\omega, T)\, d\omega, \tag{1}$$

where C is the spectral heat capacity, v_g is the phonon group velocity, ω is the angular frequency, and τ_{eff} is the total effective relaxation time.[14,15] The sum runs over all phonon polarizations. For simplification, one generic acoustic phonon branch was assumed in this work. Averaging was done over the velocity of the longitudinal ($v_{s,\text{long}}$) and the two transverse ($v_{s,\text{trans}}$) branches by $v_s = 3/(v_{s,\text{long}}^{-1} + v_{s,\text{trans1}}^{-1} + v_{s,\text{trans2}}^{-1})$.[16] Here, the Born–van Karman (BvK) model was used as the phonon dispersion relation, which determined the phonon density of states; hence, $C(\omega, T)$ and v_g, whereas τ_{eff} depended on the phonon scattering mechanisms. The BvK model described the phonon dispersion, being a sine-type,[14,17,18] as $\omega = \omega_{\max}\sin(\pi q/2q_{\max})$, where the cut-off wave vector $q_{\max} = \omega_D/v_s$ and the cut-off frequency $\omega_{\max} = 2\omega_D/\pi$. Both parameters used ω_D as the Debye cut-off frequency, which was determined by the volume of the primitive unit cell.[19] In the BvK model, dispersion v_g was calculated via $v_g = v_s\sqrt{1-(\omega/\omega_{\max})^2}$. The corresponding values for velocity calculation can be found in Table II.

The total effective phonon relaxation time combined different phonon scattering processes, such as Umklapp scattering τ_U,[20,21] point defect scattering τ_{PD},[22] which also included isotope

19 September 2024 08:56:25

© Author(s) 2024

TABLE II. Material parameters used for the model: the values were taken from Vienna *Ab initio* Simulation Package (VASP) calculations.[14]

	ρ (kg/m^3)	$v_{s,\text{trans1}}$ (m/s)	$v_{s,\text{trans2}}$ (m/s)	$v_{s,\text{long}}$ (m/s)
AlN	3201	6027	6406	10 751
$Al_{0.3}Ga_{0.7}N$	5106	4624	5118	8 502
GaN	5923	4022	4566	7 538

scattering[23,24] and grain boundary scattering τ_{GB}[25] by applying Matthiessen's rule,

$$\tau_{eff}^{-1} = \tau_U^{-1} + \tau_{PD}^{-1} + \tau_{GB}^{-1}. \tag{2}$$

These relaxation times had different dependencies on temperature and frequency,

$$\tau_U^{-1}(\omega, T) = \frac{2\, k_B \delta\, \gamma^2}{(6\pi^2)^{1/3}\, M v_p^2 v_g} \omega^2 T\, e^{-(\theta/bT)}, \tag{3}$$

$$\tau_{PD}^{-1}(\omega) = \frac{\delta^3}{4\,\pi\, v_p^2 v_g} \omega^4\, \Gamma\,, \tag{4}$$

$$\tau_{GB}^{-1}(\omega) = \frac{v_g}{\alpha D_{Avg}(0.7097(\omega_{\max}/\omega))}. \tag{5}$$

Here, δ denotes the characteristic length scale of the lattice, which is assumed as the cubic root of the atomic volume. The atomic volume, in turn, is the atomic molar mass divided by the density of the material. M stands for the average mass of an atom in the crystal, which is calculated by the division of the molar mass by the number of atoms in the unit cell. v_P represents the phonon phase velocity, v_g the phonon group velocity, and b is a constant of the vibrational spectrum of the material. In terms of reducing the fitting parameter, b was set as 3 for GaN.[26] Θ is the Debye temperature and Γ is the phonon scattering parameter. For a single element, Γ described the scattering by point defects, where $\Gamma = \Gamma_{imp}$. For isotopes, $\Gamma = \Gamma_{imp} + \Gamma_{iso}$, where Γ_{iso} defines the isotope-phonon scattering. Γ_{iso} is dependent on the difference in the mass field of the constituents and their concentration[27] and was calculated according to the equations in Ref. 24. For alloys, the scattering parameter also comprises the scattering caused by alloying (Γ_{alloy}), $\Gamma = \Gamma_{imp} + \Gamma_{iso} + \Gamma_{\text{alloy}}$.[28] Γ_{alloy} is related to the difference in mass and the lattice constants between the elements of the alloy. For τ_{GB}, the parameter D_{Avg} accounts for the average grain size of the material, and the parameter α describes the effect of boundary transmission, whereas its value is <1.[29] As we do not know both parameters, they were fitted together as one unknown variable. Γ_{alloy} and Γ_{imp} were also treated as one fitting parameter. In this study, the normal phonon scattering was ignored as it had a neglectable influence on the temperature range (25–300 °C), in which our experiments were done.[27] The material parameters used in these calculations are summarized in Table III.

Usually, the length dependency of the thermal conductivity was taken into account by an additional scattering term in Eq. (2), where the boundary scattering is $\tau_B = v_g/L$ based on Fourier's law.[27] L is the characteristic geometric restriction of the layer, which had been mostly taken as half of the thickness. In this study, we used the suppression function to describe the boundary scattering. It includes both Fourier's law and the ballistic behavior of phonons at a boundary. Hereby, in Eq. (1), the suppression function S is additionally included,

$$\kappa = \frac{1}{3} \sum_i \int C(\omega, T)\, v_g^2(\omega)\, \tau_{eff}(\omega, T)\, S(Kn(\omega))\, d\omega. \tag{6}$$

The suppression term is a function of the Knudsen number (Kn), which is $Kn(\omega) = v_g \tau_{eff(\omega)}/L$. S is analogous to the Fuchs–Sondheimer equation for the thermal conductivity,

$$S(Kn(\omega)) = 1 + 3Kn(\omega)(E_5(Kn^{-1}(\omega)) - 0.25). \tag{7}$$

E_5 is an exponential integral; more details about that can be found in the paper introducing this approach.[25]

IV. RESULTS AND DISCUSSION

A. Thermal and structural properties of GaN-HEMT stack

TDTR analysis was done sequentially, starting with S1 (200 nm AlN on Si) followed by other samples in the numbered order. Hence, the result of S1 was used as input parameters for S2, S2, S3, and so on. The measured thermal conductivity values of the 200 nm AlN (S1) at different temperatures are shown in Fig. 2. Here, the analyzed thermal conductivity was in the range of 55–75 W/mK. It has already been reported that the thermal conductivity values of bulk AlN range from 20 to 400 W/mK, depending on the grain size, vacancy concentration, oxygen contents, and crystalline lattice orientation.[31–33] Furthermore, the size effect reduced the AlN thermal conductivity; however, the theoretical prediction at the corresponding thickness is higher than the measured one due

19 September 2024 08:56:25

TABLE III. Material parameters used for the described model of lattice thermal conductivity. The parameters of AlGaN alloy were evaluated from the values of GaN and AlN with the virtual crystal model.[30]

	M (kg)	Θ (K)	ω_D (rad/s)	δ (m)	Γ_{iso}[24]	γ
AlN	3.48×10^{-26}	978.7	1.28×10^{14}	3.49×10^{-10}	4.30×10^{-6}	0.75
$Al_{0.3}Ga_{0.7}N$	5.91×10^{-26}	749.8	9.82×10^{13}	3.57×10^{-10}	1.93×10^{-4}	0.74
GaN	6.95×10^{-26}	652.0	8.54×10^{13}	3.61×10^{-10}	2.74×10^{-4}	0.73

© Author(s) 2024

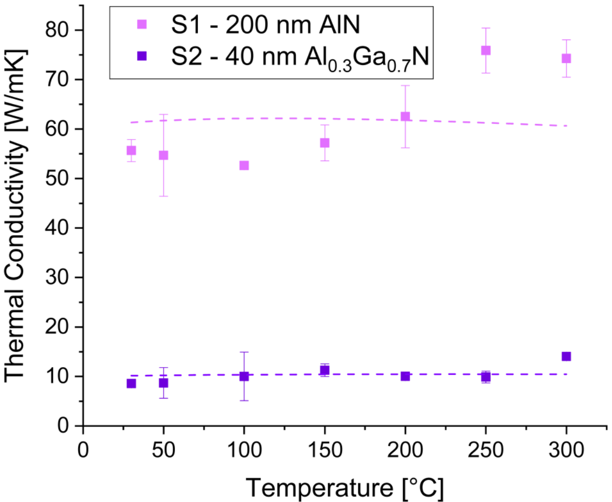

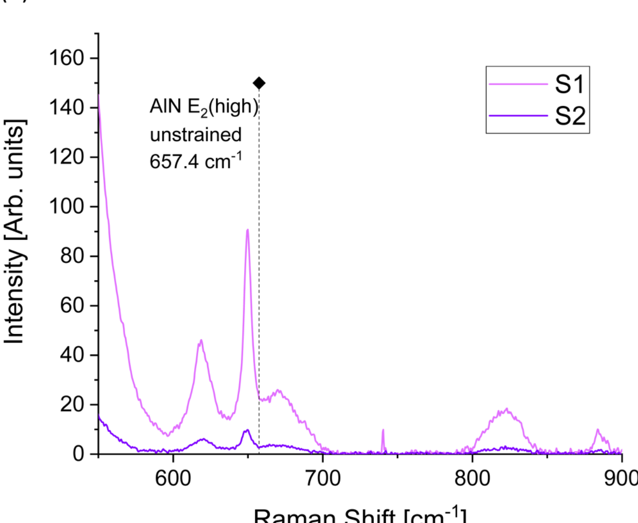

FIG. 2. (a) The analyzed thermal conductivity of 200 nm AlN and 40 nm $Al_{0.3}Ga_{0.7}N$. The dashed lines depict the BvK models for lattice thermal conductivities, describing the scattering processes in materials. (b) The corresponding Raman spectra of the layers measured at the sample surface.

to the additional scattering mechanisms.[34] Our obtained values are similar to other studies, in which AlN was either found to be polycrystalline or had an amorphous SiN transition layer between AlN and Si which could govern the measurements.[31,33,35,36] In our findings, we detected an increase in the thermal conductivity with temperature from 55 W/mK at 30 °C to 75 W/mK at 300 °C; this has been in contrast to the behavior of single crystalline AlN.[37] It was assumed that this dependency on temperature stemmed from the disordered area between Si and AlN,[38] where the temperature led to increased thermal transport.[39–41] The applied thermal transport model (see Sec. III) could not describe this increase based on a crystalline state. The fitting parameters are not in the range of pure crystalline materials. Γ_{imp} has a high value of 0.0097. This value is closer to Γ_{imp} of alloys and not to crystalline materials, which are of the order of 10^{-5} and 10^{-7}.[14,42] αD_{avg} is in the range of 10^{-8} m. Both values implied that there were dislocations and impurities, e.g., oxygen, in the investigated AlN layer, which was confirmed by Raman investigations.

The Raman spectrum of AlN consisted of the E2(high) mode at $\omega' = 649.8\ \text{cm}^{-1}$, and no other AlN-related peak was detected [see marker Fig. 2(b)]. It must be mentioned that the spectrum was dominated by the peaks of the Si substrate; hence, all other peaks in the spectra can be assigned to the Si substrate similar to Ref. 43. The position of the unstrained AlN lattice was $\omega'_0 = 657.4\ \text{cm}^{-1}$ according to Ref. 44; hence, our peak position implied the presence of stress.[45] The residual stress can be calculated by using the following equation:

$$\sigma = (\omega' - \omega'_0)/a_\sigma, \tag{8}$$

where the stress shift coefficient a_σ had a value of $-6.3\ \text{cm}^{-1}$/GPa.[46] So, a biaxial stress of 1.2 GPa was calculated for the 200 nm AlN layer grown on Si and had a tensile nature, which was comparable to the results of Ref. 47. First principle calculations have also shown that the thermal conductivity of wurtzite AlN decreases with increasing tensile stress.[48] Experimentally, it was investigated that the tensile stress was also an indicator of the grain size: the smaller the size, the higher the tensile stress.[49] This was in accordance with the findings in our thermal measurements. Furthermore, the Raman line width indicated the presence of defects (impurities, dislocations, microcracks, etc.) and the overall crystalline quality; here, a full-width half maximum (FWHM) $6\ \text{cm}^{-1}$ of E_2(high) was found. In comparison, in bulk AlN, an FWHM of $3\ \text{cm}^{-1}$ at 300 K was investigated.[33,50]

In Fig. 2(a), we show the measured thermal conductivity of the 40 nm $Al_{0.3}Ga_{0.7}N$ layer. The thermal conductivity was significantly reduced compared to AlN and GaN due to the prominent alloy scattering. It was found that $\Gamma_{alloy} + \Gamma_{imp}$, which were fitted as one parameter, has a value of 0.015, which was higher than the fitted Γ_{imp} of AlN (see Table IV). αD_{avg} showed a value of 4×10^{-9} m. Even though the thermal transport was dominated by the aforementioned scattering mechanism, the thickness of the $Al_xGa_{1-x}N$ layer also influenced the effective thermal conductivity and, hence, showed an indication of quasi-ballistic thermal transport.[14,51] According to Adachi,[52] the bulk thermal conductivity of $Al_{0.3}Ga_{0.7}N$ at 30 °C should be around 14.5 W/mK. Here, a thermal conductivity of (8.5 ± 0.5) W/mK was measured at 30 °C. A slight increase in thermal conductivity as a function of temperature can be seen here. The results were in agreement with the findings of Refs. 53 and 54.

The Raman spectrum of the S2 sample only revealed the AlN-related peak at $649.2\ \text{cm}^{-1}$ [Fig. 2(b)]. However, the alloying-induced Raman shift of AlN-like E2(high) according to Holtz *et al.*[55] should be $609\ \text{cm}^{-1}$ for $Al_{0.3}Ga_{0.7}N$. This indicated that the Raman spectrum of S2 [Fig. 2(b)] was dominated by the AlN layer and the Si substrate underneath.

19 September 2024 08:56:25

© Author(s) 2024

TABLE IV. The fitting parameters of the BvK model for different materials in the stack.

	AlN	$Al_{0.3}Ga_{0.7}N$	AlN/ AlGaN SL	GaN:C (S7–S9)	GaN (S7–S8)
Γ	0.0097	0.0153[a]	…	1.5×10^{-4}	0.0024
b	3.7	3.4	…	3	3
αD_{avg} (m)	2.2×10^{-8}	4.2×10^{-9}	…	3.34	0.97
G (W/m^2 K)	…	…	2.0×10^{-9}	…	…

[a]Γ is here ($\Gamma_{imp} + \Gamma_{alloy}$).

Samples S3–S6, superlattices with different thicknesses between 165 and 1320 nm with the same period lengths of AlN/AlGaN, were investigated thermally. The thermal conductivity values are shown in Fig. 3(a). The cross-plane thermal conductivity ~8.5 W/mK at 30 °C was in the range of the thermal conductivity of 8.3 W/mK of 12 nm AlN/12 nm GaN from Ref. 56 and 8 W/mK of the 10.6 nm $Al_{0.23}Ga_{0.77}N$/8.8 nm GaN superlattice from Ref. 57. Our results showed to have a lower thermal conductivity than the 40 nm $Al_{0.3}Ga_{0.7}N$ layer of S2, due to the interface crossing of phonons, leading to a quenching of the thermal conductivity.[57] In our study, there was no thickness-dependent trend of the superlattice layer. Regardless of the conducted measurements, they had a larger thermal penetration depth than the thickness of the superlattices. The one-dimensional assumption of the thermal penetration depth (d), which was a spatial extent of the temperature gradient, can be calculated by $d = \sqrt{\alpha/\pi f}$, where $\alpha$is the thermal diffusivity and f is the modulation frequency of 200 kHz of the TDTR. With the highest thermal diffusivity value, we calculated $d \sim 2.3\,\mu$m. Also, previous studies showed that there was no conclusive trend in the thermal conductivity with its thickness at thicknesses above 100 nm. In that thickness range, the diffusive thermal transport dictated the thermal conductivity and not the quasi-ballistic transport anymore.[58] The cross-plane thermal conductivity of the superlattice was calculated by the model proposed by Mei *et al.*[59] and applied by Filatova-Zalewska *et al.*,[57]

$$\kappa_{SL,\mathrm{cross}} = (L_{Al_{0.3}Ga_{0.7}N} + L_{AlN})\left(\frac{L_{AlGaN}}{\kappa_{AlGaN}} + \frac{L_{AlN}}{\kappa_{AlN}} + \frac{2}{G}\right)^{-1}. \quad (9)$$

In Eq. (9), L_x stands for the thicknesses of the AlGaN and AlN layers within the superlattice; hence, $L_{AlGaN} + L_{AlN}$ was the length of one period of 33 nm. The thermal conductivities of AlGaN and AlN (κ_{AlGaN} and κ_{AlN}) were calculated by the resulting model used for S1 and S2, where in Eq. (7), layer thicknesses were adopted. The thermal boundary conductance (G) was used here as a fitting parameter, resulting in $2 \times 10^9\,W/m^2K$ in the measured temperature range. Such a value was also found in previous works for AlGaN/GaN[57] and AlN/GaN.[60] By applying the TDTR measurements, the cross-plane thermal conductivity of the superlattice was mainly analyzed; however, anisotropic heat transport can be considered in the evaluation by an anisotropy factor. This anisotropy factor is shown in the inlet of Fig. 3(a). The evaluated factor lies in the range of 1.4 and 1.6 for samples S3–S5 at 30 °C. These values were in agreement with the value found for GaAs/AlAs superlattices reported by Luckyanova *et al.*[61] It was shown that the value was lower than that of the AlN/GaN superlattice, where the mass mismatch was greater and, hence, led to a higher reduction in the phonon group velocity. Only sample S6 does not show any anisotropic behavior at 30 °C and it was not so pronounced as for S3–S5 at elevated temperatures. These values could be assigned to the quality of the interfaces, which played an important role in anisotropic thermal transport. Interdiffusion at the interfaces led to more diffusive scattering and, hence, influenced the overall heat conduction.[62] This was supported by the findings of Raman measurements and the peak intensity in the spectra [Fig. 3(b)].

Raman spectra of the AlGaN/AlN superlattice are shown in Fig. 3(b). In the spectra of samples S3–S6, the E_2(high) mode is split into the AlN-related and GaN-related peaks. The FWHM of these peaks was a descriptor of the disorder of the alloy.[63] The S4 samples showed to have the sharpest E_2(high) modes for both elements, whereas the AlN-like E_2(high) mode of S6 shows a peak broadening, indicating that the interfaces between AlGaN and AlN layers were smeared out due to interdiffusion. The peak shift of the AlN-like E_2(high) mode toward lower wave numbers and vice versa for the GaN-like E_2(high) mode follows the alloying-induced peak shift. However, this shift was not as distinctive as predicted in Ref. 55 due to the superlattice and not pure alloying. Comparing the samples, the GaN-like E_2(high) mode exhibited a monotonic downward shift (max. 2.4 cm^{-1}) to the unstressed state with increasing thickness of the superlattice. In addition, a peak could also be seen at 770 cm^{-1} in the Raman spectra [Fig. 3(b)], whose peak shift of ~37 cm^{-1} stemmed from the alloying.[55]

A further thickness-dependent study was executed by samples S7–S9, investigating the thickness dependence of the C-doped GaN layers. In this study, the 250 nm GaN layer (S7) had ~34% of the thermal conductivity compared to the 1 μm GaN layer (S9) at 30 °C. This trend could be seen in other reports, e.g., Refs. 64 and 65. However, the absolute values of our study were shown to be higher (>20 W/mK) compared to the mentioned literature, which could be related to the differences in material quality due to different deposition techniques. The thermal model applied was used simultaneously for all three samples (S7–S9) with C-doped GaN on top, according to Eqs. (6) and (7), which include the thickness dependence of the thermal conductivity. This multiple-fit model is illustrated in Fig. 4(a) as solid lines. The fitting parameters in Table IV show that neither Γ_{imp} nor αD_{avg} were the governing parameters for thermal conductance. Γ_{imp} was in the range of Γ_{iso} and more than an order of magnitude smaller than Γ_{imp} of the AlN and $Al_{0.3}Ga_{0.7}N$ layers of S1 and S2. αD_{avg} was larger than the layer thickness and, hence, negligible. It could be seen that the applied model showed higher values than that measured for samples S7

19 September 2024 08:56:25

© Author(s) 2024

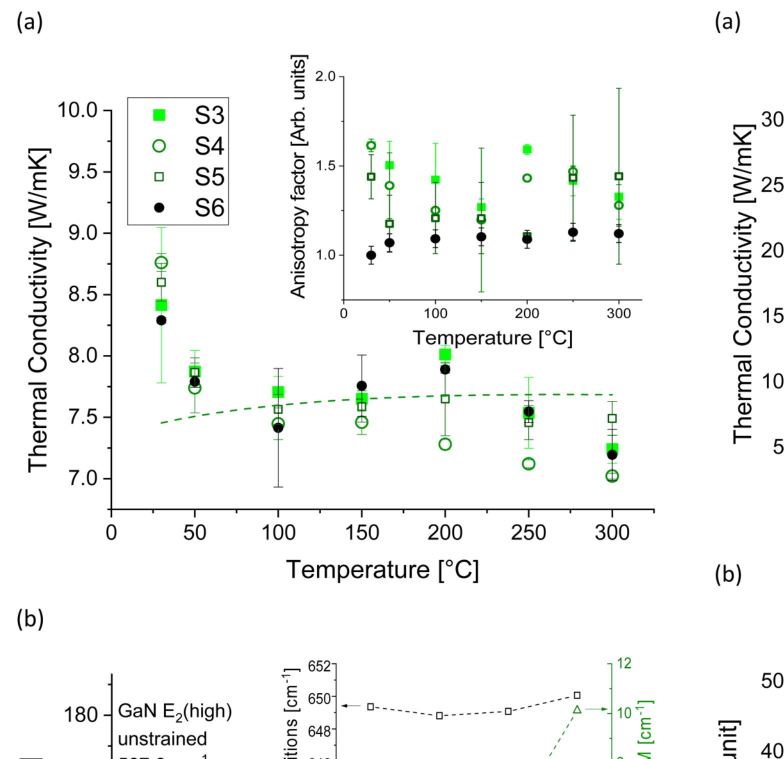

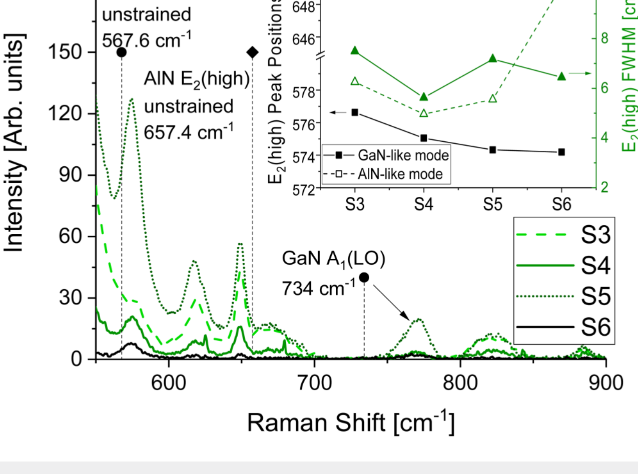

FIG. 3. (a) The obtained cross-plane thermal conductivity of the superlattice AlN/AlGaN with different overall thicknesses as a function of temperature. Inlet: The anisotropy factor of thermal conductivity as a function of temperature. (b) The Raman spectra of the superlattice (S3–S6) with a different thickness. The inlet shows the peak shift of the E_2(high) mode, whereas the GaN-related peak shift is marked as a black square and the AlN-related peak shift as an open square. The triangles present the FWHM of the E_2(high) mode.

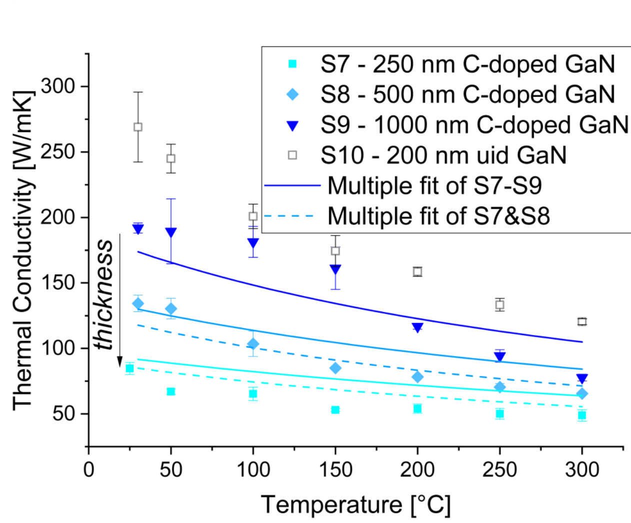

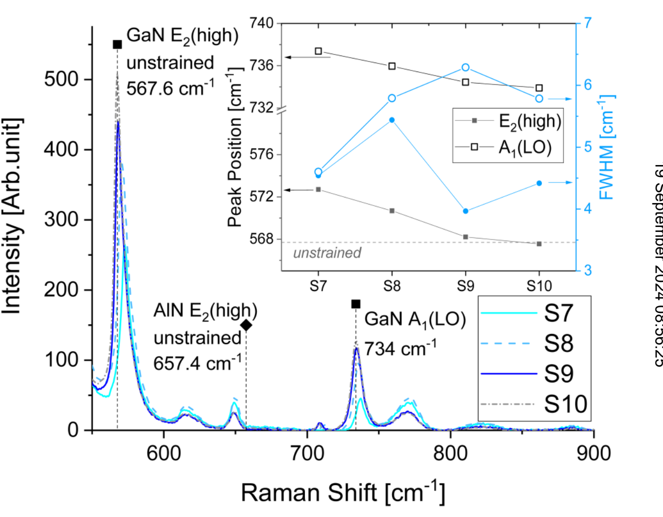

FIG. 4. (a) The thermal conductivity of C-doped GaN with different thicknesses and 200 nm uid GaN as a function of temperature. (b) The Raman spectra of samples S7–S10. The inlet presents the features of the GaN-related E_2(high) as filled markers and A_1(LO) peaks as open markers of the samples S7–S10. The peak positions are marked as black squares and their corresponding FWHM as blue cycles.

and S8. Thus, an additional multiple fit only with those samples was carried out [dashed line in Fig. 4(a)], leading to higher Γ_{imp} and lower αD_{avg} values (see Table IV). In particular, Γ_{imp} was an order of magnitude higher, which was also reflected in the FWHM of the Raman E_2(high) peak [inlet of Fig. 4(b)]. The uid GaN of S10 showed a higher thermal conductivity than the C-doped GaN. It could be assumed that the uid GaN layer was thermally not distinguishable from the C-doped GaN layer underneath. As the bulk value of undoped GaN was in the same range as our result of 269 W/mK at 30 °C,[66,67] our findings indicated that the phonons did not see any interface between uid GaN and C-doped GaN. As no additional boundary scattering happens between those layers, there was also no size-dictated effect of 200 nm recorded.

The E_2(high) mode of GaN was analyzed in more detail. For GaN, likewise, as in AlN, the residual stress could be characterized

19 September 2024 08:56:25

© Author(s) 2024

by Eq. (8). The unstrained peak for GaN was found to be 567.7 cm^{-1}[68] and a_σ had a value of −2.9 cm^{-1}/GPa.[69] S7–S9 samples were under compressive stress, which decreased from −1.7, −1.0 to −0.18 GPa with increasing thickness, respectively. The stress and its trend were in line with other studies. For example, Pavlidis *et al.*[70] and Ni *et al.*[71] showed the effect of the underlying SL on GaN stress, and Ni *et al.*[72] the influence of C-doping. According to first principle calculations, a compressive state in GaN intrinsically led to increased thermal conductivity and phonon confinement.[73] Note that this correlation is not included in our thermal transport model [Eq. (6)]. S10 was found to have a small tensile stress of 50 MPa; so, it was nearly in a stress-free state. The FWHM of the E_2(high) mode was the highest for S8 (500 nm GaN layer) followed by S7. The A1(LO) phonon mode of GaN was an indicator of the free carrier concentration. With increasing concentration, the A1 (LO) mode had a peak position shift to higher frequencies and a decrease in its intensity. According to that, S7 had the highest free carrier concentration and S10 the lowest, and the thermal conductivity does not correlate with the free carrier concentration, as the electrical contribution is negligible in GaN.[74,75]

B. Thermal resistance calculation of GaN-HEMT stack by numerical simulation

A three-dimensional model of the HEMT stack was established, according to the schematics of Fig. 1 (S10) and the obtained thermal conductivities. Thermal simulations were carried out by finite volume software.[76] There, a heat source with a width of 1 μm was placed on top of the stack, representing the gate center as an example, because it was already shown that underneath the gate, there was the highest temperature.[77–79] The numerical model had the following boundary conditions: (i) the heat source was set to 1 W,[5] and (ii) the model had adiabatic boundary conditions, except that the bottom of the Si substrate had a constant temperature (T_{HS}). As the simulation only consisted of one heat source, the heat flow in the model is assumed to be mainly in the vertical direction. This simulation study focused on the extraction of the thermal resistance under different heat sink temperatures, which is visualized in Fig. 5(a). The obtained temperature rise increased with increasing temperature due to the temperature-dependent thermal conductivity of GaN and Si. It can be seen here that the C-doped GaN layer had a dominant impact on the heat transfer of the HEMT stack, due to a higher lateral heat transfer at the top layers.[70,80] So, simulations were carried out on the stack, with varied thicknesses of C-doped GaN following the thermal measurements of samples S7–S9. In Fig. 5(b), the normalized thermal resistance is shown for all simulation models. Here, the maximal thermal resistance ($R_{th,max}$) was 158 W/mK for 250 nm GaN at 130 °C heat sink temperature, due to the reduced thermal conductivity caused by thickness reduction [see S7—Fig. 4(a)]. The temperature dependency was more pronounced for thicker GaN layers according to their thermal conductivity temperature dependency. In contrast to GaN, the reduction of the layer thickness of the superlattice affected a decrease in the thermal resistance (R_{th}) nearly proportional to the thickness, as there is no significant thickness-dependency in its thermal conductivity [see Figs. 4(a) and 5(b)]. The thickness of the SL is accompanied by increased mechanical stress in the GaN layer and also increased dislocation density. A high dislocation density in GaN is at the expense of the crystalline quality and, hence, decreased thermal conductivity and breakdown voltage.[42,81] An increased thickness of the GaN layer is in accordance with the breakdown characteristic of the device: the thicker the GaN layer, the higher the vertical breakdown voltage.[82] Our simulation revealed that—from a thermal perspective only—a HEMT device stack with a SL as thin as possible and GaN as thick as possible (until the phonon confinement limit) has the smallest R_{th} and the best thermal management. It also showed that the increased thickness of GaN has more impact on R_{th} than the reduction in the SL thickness.

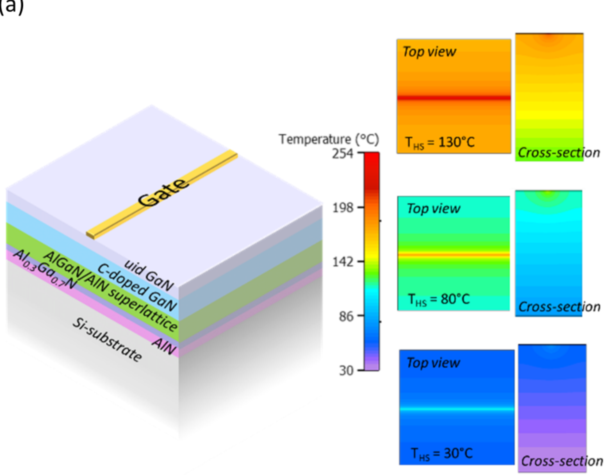

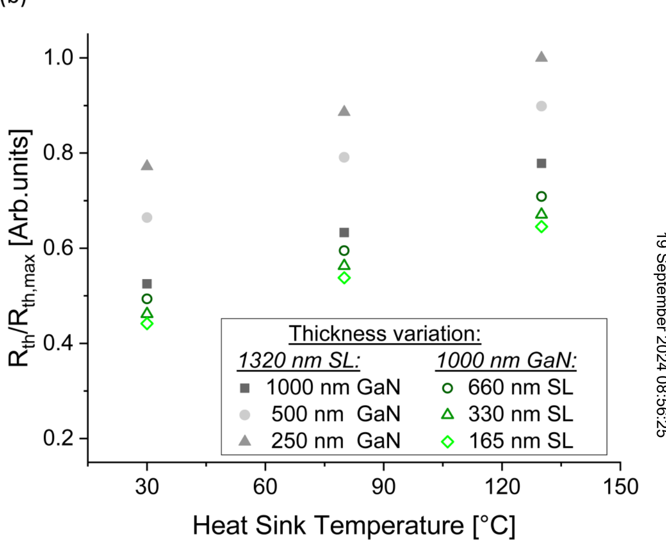

FIG. 5. (a) Steady-state simulation of a GaN-HEMT stack (like S10) at different heat sink temperatures (T_{HS}) (130, 80, and 30 °C). (b) The normalized thermal resistance as a function of heat sink temperature but also the impact of layer thickness on the thermal resistance is shown here by a varied GaN layer and superlattice thicknesses.

19 September 2024 08:56:25

© Author(s) 2024

V. CONCLUSION

In this study, thermal as well as structural analyses and their correlations of the individual materials in a GaN-HEMT stack were presented. The correlation and interpretation of these results were performed by using the Born–van Karman approach and the suppression function method. The generated thermal properties were further processed by numerical simulations, demonstrating the thermal optimum of such a GaN-HEMT stack device. Here, it was shown that the heat conduction of the AlN nucleation layer is limited mainly by phonon-grain boundary scattering and also by phonon-impurity and phonon-boundary scattering. The formation of small grains is fostered by the tensile stress in AlN grown on Si, obtained by the Raman measurements. The thermal transport in the 40 nm $Al_{0.3}Ga_{0.7}N$ is hindered substantially by alloy scattering but it was also shown that in these materials, the size effect was still evident. Contrary to the AlN/AlGaN superlattice, where no size effect was detected, here, there was a further reduced thermal conductivity due to its high interface density. Additionally, an anisotropy in thermal conductivity was measured in the superlattice, whose value depended on the quality of the interface and its potential interdiffusion. Furthermore, thermal transport in the C-doped GaN layer was limited by phonon–phonon scattering but not by impurity and grain boundary scattering, which increased the impact of the layer thickness on the thermal conductivity. It has been shown that the thermal conductivity decreases by more than 60% from 250 to 1000 nm thickness. The GaN layers with a smaller thickness exhibited more impurities, enhancing the thermal conductivity reduction, even though the detected compressive stress, which decreases with increasing layer thickness, promoted high thermal conductivity. The uid GaN layer on top ended up with a nearly stress-free state of 50 MPa tensile stress. Finally, a 3D numerical thermal model was constructed to study the temperature distribution and the thermal resistance of such an HEMT stack. The simulation results in terms of thermal management showed that GaN in a few hundred nm range could cause thermal issues and overheating in the device. This can limit their usage in high-power applications. From a thermal perspective, it can be said that the thicker the GaN layer, the better the heat dissipation according to the increased thermal conductivity and the lateral heat flow. This is in contrast to the superlattice layer, where the reduction of its thickness can decrease the thermal resistance. The outcome of our study should provide an insight into the thermal transport mechanisms of the individual layers and their optimization potential in terms of the production process and, hence, improved thermal conductivity. The study should also point out the importance of using appropriate thermal conductivity values for modeling and designing transistor devices, as the bulk values underestimate the arising thermal resistance. The paper should support designing proper thermal management in GaN-based microelectronic devices.

SUPPLEMENTARY MATERIAL

See the supplementary material for input parameter for TDTR modeling and tables with the used thermal parameters for the evaluation of thermal conductivity and modeling.

ACKNOWLEDGMENTS

This project has received funding from the ECSEL Joint Undertaking (JU) under Grant Agreement No. 876659. The JU receives support from the European Union's Horizon 2020 research and innovation programme Germany, Austria (BMK-IKT der Zukunft, FFG Project No. 877534), Slovakia, Sweden, Finland, Belgium, Italy, Spain, Netherlands, Slovenia, Greece, France, and Turkey. The document reflects only the authors' views and the JU is not responsible for any use that may be made of the information it contains.

AUTHOR DECLARATIONS

Conflict of Interest

The authors have no conflicts to disclose.

Author Contributions

Lisa Mitterhuber: Conceptualization (lead); Data curation (lead); Formal analysis (lead); Funding acquisition (supporting); Investigation (lead); Methodology (equal); Visualization (lead); Writing – original draft (lead); Writing – review & editing (equal). **Barbara Kosednar-Legenstein:** Data curation (supporting); Formal analysis (supporting); Investigation (supporting); Methodology (supporting); Visualization (supporting); Writing – review & editing (equal). **Anurag Vohra:** Data curation (supporting); Formal analysis (supporting); Resources (supporting); Validation (supporting); Writing – review & editing (equal). **Matteo Borga:** Conceptualization (supporting); Formal analysis (supporting); Funding acquisition (equal); Project administration (equal); Writing – review & editing (supporting). **Niels Posthuma:** Funding acquisition (equal); Project administration (equal); Resources (equal); Supervision (equal); Writing – review & editing (supporting). **Elke Kraker:** Conceptualization (supporting); Formal analysis (supporting); Funding acquisition (equal); Project administration (equal); Resources (equal); Supervision (equal); Writing – review & editing (equal).

19 September 2024 08:56:25

DATA AVAILABILITY

The data that support the findings of this study are available from the corresponding author upon reasonable request.

REFERENCES

[1] J. A. del Alamo and J. Joh, "GaN HEMT reliability," Microelectron. Reliab. **49**(9–11), 1200–1206 (2009).
[2] A. Kalavagunta, S. Mukherjee, R. Reed, and R. D. Schrimpf, "Comparison between trap and self-heating induced mobility degradation in AlGaN/GaN HEMTs," Microelectron. Reliab. **54**(3), 570–574 (2014).
[3] K. Ranjan, S. Arulkumaran, G. I. Ng, and A. Sandupatla, "Investigation of self-heating effect on DC and RF performances in AlGaN/GaN HEMTs on CVD-diamond," IEEE J. Electron Devices Soc. **7**, 1264–1269 (2019).
[4] J. Joh, J. A. Del Alamo, U. Chowdhury, T. M. Chou, H. Q. Tserng, and J. L. Jimenez, "Measurement of channel temperature in GaN high-electron mobility transistors," IEEE Trans. Electron Devices **56**(12), 2895–2901 (2009).
[5] A. Jakani, R. Sommet, F. Gaillard, and J. C. Nallatamby, "Comparison of GaN HEMTs thermal results through different measurements methodologies: Validation with 3D simulation," in *2021 27th International Workshop*

© Author(s) 2024

on Thermal Investigations of ICs and Systems (THERMINIC 2021) (IEEE, 2021), pp. 1–4.
[6]H. Wang *et al.*, "Investigation on the thermal characteristics of enhancement mode p-GaN HEMT device on Si substrate using thermoreflectance microscopy," Micromachines **13**(3), 4–11 (2022).
[7]A. Sarua *et al.*, "Thermal boundary resistance between GaN and substrate in AlGaN/GaN electronic devices," IEEE Trans. Electron Devices **54**(12), 3152–3158 (2007).
[8]D. Kosemura, V. Sodan, and I. D. Wolf, "Correlation between temperature dependence of Raman shifts and in-plane strains in an AlGaN/GaN stack," J. Appl. Phys. **121**(3), 035702 (2017).
[9]M. Kuball and J. W. Pomeroy, "A review of Raman thermography for electronic and opto-electronic device measurement with submicron spatial and nanosecond temporal resolution," IEEE Trans. Device Mater. Reliab. **16**(4), 667–684 (2016).
[10]C. Song, J. Kim, H. Lee, and J. Cho, "Fundamental limits for near-junction conduction cooling of high power GaN-on-diamond devices," Solid State Commun. **295**(September 2018), 12–15 (2019).
[11]T. Batten, J. W. Pomeroy, M. J. Uren, T. Martin, and M. Kuball, "Simultaneous measurement of temperature and thermal stress in AlGaN/GaN high electron mobility transistors using Raman scattering spectroscopy," J. Appl. Phys. **106**(9), 3–7 (2009).
[12]X. Zhu, J. Ma, T. Huang, M. Li, K. M. Wong, and K. M. Lau, "Improved surface morphology and mobility of AlGaN/GaN HEMT grown on silicon substrate," Phys. Status Solidi C **9**(3–4), 473–475 (2012).
[13]D. G. Cahill, "Analysis of heat flow in layered structures for time-domain thermoreflectance," Rev. Sci. Instrum. **75**(12), 5119–5122 (2004).
[14]L. Mitterhuber, R. Hammer, T. Dengg, and J. Spitaler, "Thermal characterization and modelling of AlGaN-GaN multilayer structures for HEMT applications," Energies **13**(9), 2363 (2020).
[15]A. Jacquot, B. Bayer, M. Winkler, and M. Jaegle, "Coupled theoretical interpretation and experimental investigation of the lattice thermal conductivity of Bi_2Te_3 single crystal," AIP Conf. Proc. **1449**, 61–64 (2012).
[16]B. Jugdersuren *et al.*, "Thermal conductivity of amorphous and nanocrystalline silicon films prepared by hot-wire chemical-vapor deposition," Phys. Rev. B **96**(1), 1–8 (2017).
[17]C. E. Dames, "Thermal properties of nanowires and nanotubes: Modeling and experiments," Ph.D. thesis (Department of Mechanical Engineering, Massachusetts Institute of Technology, 2007).
[18]E. S. Toberer, A. Zevalkink, and G. J. Snyder, "Phonon engineering through crystal chemistry," J. Mater. Chem. **21**(40), 15843–15852 (2011).
[19]F. Yang and C. Dames, "Heating-frequency-dependent thermal conductivity: An analytical solution from diffusive to ballistic regime and its relevance to phonon scattering measurements," Phys. Rev. B **91**(16), 165311–165325 (2015).
[20]J. Callaway, "Model for lattice thermal conductivity at low temperatures," Phys. Rev. **113**(4), 1046–1051 (1959).
[21]R. Peierls, "Zur kinetischen Theorie der Wärmeleitung in Kristallen," Ann. Phys. **395**(8), 1055–1101 (1929).
[22]B. Abeles, "Lattice thermal conductivity of disordered semiconductor alloys at high temperatures," Phys. Rev. **131**(5), 1906–1911 (1963).
[23]P. G. Klemens and R. K. Williams, "Thermal conductivity of metals and alloys," Int. Met. Rev. **31**(1), 197–215 (1986).
[24]D. T. Morelli, J. P. Heremans, and G. A. Slack, "Estimation of the isotope effect on the lattice thermal conductivity of group IV and group III-V semiconductors," Phys. Rev. B **66**(19), 1953041–1953049 (2002).
[25]C. Hua and A. J. Minnich, "Semi-analytical solution to the frequency-dependent Boltzmann transport equation for cross-plane heat conduction in thin films," J. Appl. Phys. **117**(17), 175306 (2015).
[26]C. J. Glassbrenner and G. A. Slack, "Thermal conductivity of silicon and germanium from 3 K to the melting point," Phys. Rev. **134**(4A), A1058–A1069 (1964).
[27]M. Asen-Palmer *et al.*, "Thermal conductivity of germanium crystals with different isotopic compositions," Phys. Rev. B **56**(15), 9431–9447 (1997).
[28]W. Liu and A. A. Balandin, "Thermoelectric effects in wurtzite GaN and $Al_xGa_{1-x}N$ alloys," J. Appl. Phys. **97**(12), 123705 (2005).
[29]Z. Wang, J. E. Alaniz, W. Jang, J. E. Garay, and C. Dames, "Thermal conductivity of nanocrystalline silicon: Importance of grain size and frequency-dependent mean free paths," Nano Lett. **11**(6), 2206–2213 (2011).
[30]W. Liu and A. A. Balandin, "Temperature dependence of thermal conductivity of AI_xGa_{1-x} thin films measured by the differential 3ω technique," Appl. Phys. Lett. **85**(22), 5230–5232 (2004).
[31]C. Duquenne, M. P. Besland, P. Y. Tessier, E. Gautron, Y. Scudeller, and D. Averty, "Thermal conductivity of aluminium nitride thin films prepared by reactive magnetron sputtering," J. Phys. D: Appl. Phys. **45**(1), 015301 (2012).
[32]B. E. Belkerk, A. Soussou, M. Carette, M. A. Djouadi, and Y. Scudeller, "Structural-dependent thermal conductivity of aluminium nitride produced by reactive direct current magnetron sputtering," Appl. Phys. Lett. **101**(15), 1–5 (2012).
[33]Y. Song *et al.*, "Growth-microstructure-thermal property relations in AlN thin films," J. Appl. Phys. **132**(17), 1–42 (2022).
[34]R. L. Xu *et al.*, "Thermal conductivity of crystalline AlN and the influence of atomic-scale defects," J. Appl. Phys. **126**(18), 185105 (2019).
[35]J. Jaramillo-Fernandez, J. Ordonez-Miranda, E. Ollier, and S. Volz, "Tunable thermal conductivity of thin films of polycrystalline AlN by structural inhomogeneity and interfacial oxidation," Phys. Chem. Chem. Phys. **17**(12), 8125–8137 (2015).
[36]V. Moraes *et al.*, "Thermal conductivity and mechanical properties of AlN-based thin films," J. Appl. Phys. **119**(22), 225304 (2016).
[37]G. A. Slack, R. A. Tanzilli, R. O. Pohl, and J. W. Vandersande, "The intrinsic thermal conductivity of AIN," J. Phys. Chem. Solids **48**(7), 641–647 (1987).
[38]W. Wang, W. Yang, Z. Liu, H. Wang, L. Wen, and G. Li, "Interfacial reaction control and its mechanism of AlN epitaxial films grown on Si(111) substrates by pulsed laser deposition," Sci. Rep. **5**(June), 1–12 (2015).
[39]D. Kotchetkov and A. A. Balandin, "Modeling of thermal conductivity of polycrystalline GaN films," Mater. Res. Soc. Symp. Proc. **764**, 215–220 (2003).
[40]G. Radtke, M. Couillard, G. A. Botton, D. Zhu, and C. J. Humphreys, "Structure and chemistry of the Si(111)/AlN interface," Appl. Phys. Lett. **100**(1), 2012–2015 (2012).
[41]G. W. Auner, F. Jin, V. M. Naik, and R. Naik, "Microstructure of low temperature grown AIN thin films on Si(111)," J. Appl. Phys. **85**(11), 7879–7883 (1999).
[42]K. Park and C. Bayram, "Impact of dislocations on the thermal conductivity of gallium nitride studied by time-domain thermoreflectance," J. Appl. Phys. **126**(18), 185103 (2019).
[43]J. Jeong, K. Jang, H. S. Lee, G. S. Chung, and G.-Y. Kim, "Raman scattering studies of polycrystalline 3C-SiC deposited on SiO_2 and AlN thin films," Physica B **404**(1), 7–10 (2009).
[44]V. Y. Davydov *et al.*, "Phonon dispersion and Raman scattering in hexagonal GaN and AlN," Phys. Rev. B **58**(19), 12899–12907 (1998).
[45]X. Li, C. Zhou, G. Jiang, and J. You, "Raman analysis of aluminum nitride at high temperature," Mater. Charact. **57**(2), 105–110 (2006).
[46]T. Prokofyeva *et al.*, "Vibrational properties of AlN grown on (111)-oriented silicon," Phys. Rev. B **63**(12), 1–7 (2001).
[47]A. Severino and F. Iucolano, "Impact of growth conditions on stress and quality of aluminum nitride (AlN) thin buffer layers," Phys. Status Solidi B **253**(5), 801–808 (2016).
[48]G. Yang, Y.-B. Liu, L. Yang, and B.-Y. Cao, "Machine-learned atomic cluster expansion potentials for fast and quantum-accurate thermal simulations of wurtzite AlN," J. Appl. Phys. **135**(8), 085105 (2024).
[49]I. Simsek, G. Yolcu, M. N. Koçak, K. Pürlü, I. Altuntas, and I. Demir, "Nucleation layer temperature effect on AlN epitaxial layers grown by metalorganic vapour phase epitaxy," J. Mater. Sci. Mater. Electron. **32**(20), 25507–25515 (2021).
[50]M. Kuball, J. M. Hayes, Y. Shi, and J. H. Edgar, "Phonon lifetimes in bulk AlN and their temperature dependence," Appl. Phys. Lett. **77**(13), 1958–1960 (2000).
[51]Y. R. Koh *et al.*, "Quasi-ballistic thermal transport in $Al_{0.1}Ga_{0.9}N$ thin film semiconductors," Appl. Phys. Lett. **109**(24), 1–6 (2016).
[52]S. Adachi, "Lattice thermal conductivity of group-IV and III-V semiconductor alloys," J. Appl. Phys. **102**(6), 063502 (2007).

19 September 2024 08:56:25

© Author(s) 2024

[53]B. C. Daly, H. J. Maris, A. V. Nurmikko, M. Kuball, and J. Han, "Optical pump-and-probe measurement of the thermal conductivity of nitride thin films," J. Appl. Phys. **92**(7), 3820–3824 (2002).
[54]M. J. Slomski, *Thermal Conductivity of Group-III Nitrides and Oxides* (North Carolina State University, 2017).
[55]M. Holtz *et al.*, "Composition dependence of the optical phonon energies in hexagonal $Al_xGa_{1-x}N$," J. Appl. Phys. **89**(12), 7977–7982 (2001).
[56]A. Spindlberger, D. Kysylychyn, L. Thumfart, R. Adhikari, A. Rastelli, and A. Bonanni, "Cross-plane thermal conductivity of GaN/AlN superlattices," Appl. Phys. Lett. **118**(6), 062105 (2021).
[57]A. Filatova-Zalewska *et al.*, "Anisotropic thermal conductivity of AlGaN/GaN superlattices," Nanotechnology **32**(7), 075707 (2021).
[58]R. Cheaito *et al.*, "Interplay between total thickness and period thickness in the phonon thermal conductivity of superlattices from the nanoscale to the microscale: Coherent versus incoherent phonon transport," Phys. Rev. B **97**(8), 1–7 (2018).
[59]S. Mei and I. Knezevic, "Thermal conductivity of III-V semiconductor superlattices." J. Appl. Phys. **118**(17), 175101 (2015).
[60]Y. K. Koh, Y. Cao, D. G. Cahill, and D. Jena, "Heat-transport mechanisms in superlattices," Adv. Funct. Mater. **19**(4), 610–615 (2009).
[61]M. N. Luckyanova *et al.*, "Anisotropy of the thermal conductivity in GaAs/AlAs superlattices," Nano Lett. **13**(9), 3973–3977 (2013).
[62]P. Chen *et al.*, "Role of surface-segregation-driven intermixing on the thermal transport through planar Si/Ge superlattices," Phys. Rev. Lett. **111**(11), 1–6 (2013).
[63]C. Hodges, J. Anaya Calvo, S. Stoffels, D. Marcon, and M. Kuball, "AlGaN/GaN field effect transistors for power electronics—Effect of finite GaN layer thickness on thermal characteristics," Appl. Phys. Lett. **103**(20), 202108 (2013).
[64]F. Mu *et al.*, "High thermal boundary conductance across bonded heterogeneous GaN-SiC interfaces," ACS Appl. Mater. Interfaces **11**(36), 33428–33434 (2019).
[65]E. Ziade, J. Yang, G. Brummer, D. Nothern, T. Moustakas, and A. J. Schmidt, "Thickness dependent thermal conductivity of gallium nitride," Appl. Phys. Lett. **110**(3), 031903 (2017).
[66]K. Jagannadham, E. A. Berkman, and N. Elmasry, "Thermal conductivity of semi-insulating, p-type, and n-type GaN films on sapphire," J. Vac. Sci. Technol. A **26**(3), 375–379 (2008).
[67]H. Shibata *et al.*, "High thermal conductivity of gallium nitride (GaN) crystals grown by HVPE process," Mater. Trans. **48**(10), 2782–2786 (2007).
[68]C. J. Bong, C. W. Ahn, S. B. Bae, and E. K. Kim, "Structural characteristics and defect states of intrinsic GaN epi-layers in a high power device structure," J. Korean Phys. Soc. **79**(1), 57–63 (2021).
[69]F. Demangeot, J. Frandon, M. A. Renucci, O. Briot, B. Gil, and R. L. Aulombard, "Raman determination of phonon deformation potentials in α-GaN," Solid State Commun. **100**(4), 207–210 (1996).
[70]G. Pavlidis *et al.*, "Thermal performance of GaN/Si HEMTs using near-bandgap thermoreflectance imaging," IEEE Trans. Electron Devices **67**(3), 822–827 (2020).
[71]Y. Ni *et al.*, "Effect of AIN/GaN superlattice buffer on the strain state in GaN-on-Si(111) system," Jpn. J. Appl. Phys. **54**(1), 015505 (2015).
[72]Y. Ni *et al.*, "Dependence of carbon doping concentration on the strain-state and properties of GaN grown on Si substrate," Superlattices Microstruct. **120**(June), 720–726 (2018).
[73]D. S. Tang, G. Z. Qin, M. Hu, and B. Y. Cao, "Thermal transport properties of GaN with biaxial strain and electron-phonon coupling," J. Appl. Phys. **127**(3), 035102 (2020).
[74]Y. Song *et al.*, "The doping dependence of the thermal conductivity of bulk gallium nitride substrates," J. Electron. Packag. Trans. ASME **142**(4), 1–10 (2020).
[75]D. I. Florescu *et al.*, "Thermal conductivity of fully and partially coalesced lateral epitaxial overgrown GaN/sapphire (0001) by scanning thermal microscopy," Appl. Phys. Lett. **77**(10), 1464–1466 (2000).
[76]Siemens (Ed.), "Simcenter Flotherm Software" (2022), see https://plm.sw.siemens.com/de-DE/simcenter/fluids-thermal-simulation/flotherm/.
[77]C. Guo, J. Meng, Z. Liao, S. Feng, X. Wang, and L. Luo, "Influence of heat source size on thermal resistance of AlGaN/GaN HEMT," in *Proceedings of International Conference on ASIC* (IEEE, 2017), Vol. 2017, pp. 299–302,
[78]Q. Hao, H. Zhao, Y. Xiao, and M. B. Kronenfeld, "Electrothermal studies of GaN-based high electron mobility transistors with improved thermal designs," Int. J. Heat Mass Transfer **116**, 496–506 (2018).
[79]J. Wu, J. Min, W. Lu, and P. K. L. Yu, "Thermal resistance extraction of AlGaN/GaN depletion-mode HEMTs on diamond," J. Electron. Mater. **44**(5), 1275–1280 (2015).
[80]A. Chvála *et al.*, "Advanced characterization techniques and analysis of thermal properties of AlGaN/GaN multifinger power HEMTs on SiC substrate supported by three-dimensional simulation," J. Electron. Packag. Trans. ASME **141**(3), 031007 (2019).
[81]Z. Chen *et al.*, "Influence of the AlN/GaN superlattices buffer thickness on the electrical properties of AlGaN/GaN HFET on Si substrate," in *2016 International Forum on Wide Bandgap Semiconductors China, IFWS 2016—Conference Proceedings* (IEEE, 2016), Vol. 1, pp. 89–92.
[82]T. Egawa, "Heteroepitaxial growth and power electronics using AlGaN/GaN HEMT on Si," in *Technical Digest—International Electron Devices Meeting (IEDM)* (IEEE, 2012), pp. 27.1.1–27.1.4.

19 September 2024 08:56:25

© Author(s) 2024